This article has been accepted for publication in a future issue of this journal, but has not been fully edited. Content may change prior to final publication. Citation information: DOI 10.1109/TMI.2016.2536779, IEEE Transactions on Medical Imaging

Real-time Model-based Inversion in Cross-sectional Optoacoustic Tomography

Lu Ding, Xosé Luís Deán-Ben, and Daniel Razansky*

***Abstract*—Analytical (closed-form) inversion schemes have been the standard approach for image reconstruction in optoacoustic tomography due to their fast reconstruction abilities and low memory requirements. Yet, the need for quantitative imaging and artifact reduction has led to the development of more accurate inversion approaches, which rely on accurate forward modeling of the optoacoustic wave generation and propagation. In this way, multiple experimental factors can be incorporated, such as the exact detection geometry, spatio-temporal response of the transducers, and acoustic heterogeneities. The model-based inversion commonly results in very large sparse matrix formulations that require computationally extensive and memory demanding regularization schemes for image reconstruction, hindering their effective implementation in real-time imaging applications. Herein, we introduce a new discretization procedure for efficient model-based reconstructions in two-dimensional optoacoustic tomography that allows for parallel implementation on a graphics processing unit (GPU) with a relatively low numerical complexity. By on-the-fly calculation of the model matrix in each iteration of the inversion procedure, the new approach results in imaging frame rates exceeding 10Hz, thus enabling real-time image rendering using the model-based approach.**

***Index Terms*—optoacoustic tomography, photoacoustic tomography, model-based reconstruction, real-time imaging**

I. Introduction

Much like other tomographic imaging modalities, optoacoustic tomography (OAT) relies upon a mathematical reconstruction procedure to render images of biological samples. The algorithm employed strongly influences the imaging performance, affecting a number of parameters, which include image contrast, spatial and temporal resolution, severeness of image artifacts, and overall image quantification abilities.

Several approaches have been suggested for tomographic image reconstruction in OAT [1]–[12]. The reconstruction performance may vary in each case depending on the exact tomographic configuration employed as well as on acoustic properties of the imaged volume [8]–[11], [13]–[15]. Although analytical (closed-form) inversion algorithms, such as filtered back-projection [2], may generally result in fast and memory-efficient reconstructions, model-based approaches based on numerical (or semi-analytical) inversion of an optoacoustic forward model provide extra flexibility in terms of their applicability to different types of imaging systems and samples [10], [11]. In this way, one could for instance account for specific experimental and modeling imperfections, such as spatially-dependent response of the ultrasound transducers [9], [16], [17] or acoustic heterogeneities and attenuation in the sample and the surrounding medium [18]–[20].

Model-based reconstruction methods based on the time-domain optoacoustic wave equation are typically associated to large sparse matrix formulations. The main operations in the iterative inversion procedure are the multiplication of vectors with the model matrix and its transpose. Even though the model matrix is sparse, the large dimensionality of the problem leads to a significant computational complexity and memory overhead. Several approaches have been introduced to reduce both the computational operations and the memory requirements of model-based inversions. For example, it has been shown that the forward model can be significantly simplified in a cross-sectional acquisition geometry by assuming that the optoacoustic sources lie in a plane [21]. Thereby, the resulting two-dimensional model matrix can readily be stored in memory, in a way that fast inversion can be achieved with standard inversion algorithms. A discrete wavelet packet decomposition can be used to further speed up the computations, since the inversion is decoupled into smaller subproblems [22], although memory requirements are not significantly reduced. Both the computational complexity and memory overhead can be reduced by decreasing the number of measurements (projections) and applying appropriate regularization for sparse recovery [23]. On the other hand, inherent symmetries of the acquisition setup can be exploited to reduce the necessary memory [24]–[26]. Alternatively, the memory requirements can be drastically reduced by on-the-fly calculating the matrix vector products without explicitly storing the model matrix [27]. Efficient parallel implementation of this approach on a graphics processing units (GPU) is then feasible, so that the reconstruction time can be substantially accelerated in the same way as in other reconstruction methods [28]. Recently, other reconstruction approaches based on efficient sparse decomposition of the sequence of acquired signals have also been shown to significantly accelerate model-based reconstructions when handling multi-frame data [29], [30]. However, real-time visualization implies image reconstruction between the subsequent laser pulses, which cannot be achieved if multiple frames need to be accumulated prior to image rendering.

The proposed method drastically reduces the computational complexity of on-the-fly calculations of the matrix-vector products by storing a small table of precalculated values. The new approach then results in imaging frame rates exceeding 10Hz, thus enabling real-time image rendering using a model-

The authors are with the Institute for Biological and Medical Imaging, Technical University of Munich and Helmholtz Center Munich, Ingolstädter Landstraße 1, 85764 Neuherberg, Germany. *e-mail: dr@tum.de.

based inversion method. Note that the term real time is usually employed in optoacoustics to refer to the capability to reconstruct images with no significant delay between data acquisition and image display, even for acquisition times larger than 1 s [31], [32]. Additionally, 10 Hz represents the optimal frame rate for attaining the best signal-to-noise performance while staying below the maximum permissible laser exposure limits, namely 20 mJ/cm^2 energy density per pulse and 200 mW/cm^2 average power density. For pulse repetition rates higher than 10 Hz, the energy per pulse must then be reduced, leading to a suboptimal signal-to-noise performance [33].

II. Methods

A. The forward model

For short-pulsed laser illumination fulfilling the so-called thermal confinement conditions [34], a Dirac's delta function can be assumed to closely resemble the temporal profile of the light intensity, in which case the optoacoustically-generated pressure wave follows the following equation [35], [36]

$$\frac{\partial^2 p(\boldsymbol{r},t)}{\partial t^2} - c^2\nabla^2 p(\boldsymbol{r},t) = \Gamma H(\boldsymbol{r})\frac{\partial \delta(t)}{\partial t}, \tag{1}$$

being Γ the dimensionless Grüneisen parameter, c the speed of sound in the medium and $H(\boldsymbol{r})$ the amount of energy absorbed in the tissue per unit volume. An exact analytical solution of (1) is subsequently given by the Poisson-type integral as [35], [37]

$$p(\boldsymbol{r}',t) = \frac{\Gamma}{4\pi c}\frac{\partial}{\partial t}\int\limits_{S} \frac{H(\boldsymbol{r})}{|\boldsymbol{r}'-\boldsymbol{r}|} dS(t), \tag{2}$$

where the integral is performed along a spherical surface $S(t)$ defined as $|\boldsymbol{r}'-\boldsymbol{r}| = ct$. In cross-sectional tomography, the optoacoustic sources are assumed to lie in the same plane as the measurement points, in which case (2) is reduced into a two dimensional formulation [21], i.e.

$$p(\boldsymbol{r}',t) = \frac{\partial}{\partial t}\int\limits_{L(t)} \frac{H(\boldsymbol{r})}{|\boldsymbol{r}'-\boldsymbol{r}|} dL(t), \tag{3}$$

where $L(t)$ denotes a circumference for which $|\boldsymbol{r}'-\boldsymbol{r}| = ct$. Note that the latter equation is expressed in arbitrary units after neglecting all the constant terms.

B. Discretization on a Cartesian grid

In order to discretely represent the temporal profiles of the measured pressure signals, one may define a regular Cartesian grid covering all the optoacoustic sources in the imaged volume, as depicted by solid circles in Fig. 1 a). Each point in the Cartesian grid represents one single pixel of a two dimensional image corresponding to the distribution of the absorbed optical energy. According to (3), the pressure signal at the transducer location $\boldsymbol{r}' = (x', y')$ and time instant t equals to the derivative of the integral of the absorption distribution on an arc, as shown in Fig. 1 a). The absorption at an arbitrary location $\boldsymbol{r}$ within the grid can be subsequently interpolated from the known absorption values at the pixel points. Thus, (3) can be approximated via

$$\begin{aligned} p(\boldsymbol{r}',t) &= \frac{\partial}{\partial t}\int\limits_{L(t)} \frac{\sum\limits_i H(r_i)K(\boldsymbol{r}-\boldsymbol{r}_i)}{|\boldsymbol{r}'-\boldsymbol{r}|} dL(t) \\ &= \sum_i H(r_i)\frac{\partial}{\partial t}\left(\frac{1}{ct}\int\limits_{L(t)} K(\boldsymbol{r}-\boldsymbol{r}_i) dL(t)\right), \end{aligned} \tag{4}$$

where $K(\boldsymbol{r}-\boldsymbol{r}_i)$ is the interpolation function, i.e., the contribution of the pixel at location $\boldsymbol{r}_i$ to the optical absorption at location $\boldsymbol{r}$. Accordingly, we define

$$p_i(\boldsymbol{r}',t) = \frac{\partial}{\partial t}\left(\frac{1}{ct}\int\limits_{L(t)} K(\boldsymbol{r}-\boldsymbol{r}_i) dL(t)\right) \tag{5}$$

as the pressure contribution of the ith pixel to the pressure signal $p(\boldsymbol{r}',t)$, which can be further expressed as

$$p(\boldsymbol{r}',t) = \sum_i H(r_i) p_i(\boldsymbol{r}',t). \tag{6}$$

In the following subsections, we introduce two different interpolation models to calculate $p_i(\boldsymbol{r}',t)$ when the pixel size is much smaller than the distance ct travelled by the optoacoustic wave. In general, many interpolation methods are applicable within the framework of the suggested reconstruction approach, each exhibiting a different trade-off between accuracy and computational complexity. In this work, we used the standard bilinear interpolation method and a simpler approach, termed "circular interpolation", mainly in order to optimize the reconstruction runtime.

1) Bilinear interpolation: The absorbed energy at an arbitrary location $H(\boldsymbol{r}) = H(x,y)$ can be calculated as a function of the absorption at its 4 neighboring pixels by using bilinear interpolation. In this way, pixel i only contributes to the absorption distribution in an area within the 4 neighboring grid points (Fig. 1 b)). The interpolation function is then given by

$$K(\boldsymbol{r}-\boldsymbol{r}_i) = \begin{cases} 0 & \text{for } \|\boldsymbol{r}-\boldsymbol{r}_i\|_\infty \geqslant \Delta xy \\ \widetilde{K} & \text{for } \|\boldsymbol{r}-\boldsymbol{r}_i\|_\infty < \Delta xy \end{cases}, \tag{7}$$

where

$$\widetilde{K} = \left(1 - \frac{|x-x_i|}{\Delta xy}\right)\left(1 - \frac{|y-y_i|}{\Delta xy}\right), \tag{8}$$

and Δxy is the corresponding grid width.

Let the distance between the measuring location $\boldsymbol{r}'$ and the pixel position $\boldsymbol{r}_i$ be denoted by s. Considering a grid size Δxy much smaller than s, the integral in (5) can be approximated as the integral along a straight line in the square region for which $K(\boldsymbol{r}-\boldsymbol{r}_i)$ is not zero, as illustrated in Fig. 1 c). We define d as the distance from $\boldsymbol{r}_i$ to the integration line and α as the angle with respect to the horizontal axis [cf. Fig. 1 c)]. Since $d = s - ct$, one may rewrite (5) as

$$p_i(\boldsymbol{r}',t) = -c\frac{\partial}{\partial d}\left[\left(\frac{1}{s-d}\right)\int\limits_{L(t)} K(\boldsymbol{r}-\boldsymbol{r}_i) dL(t)\right], \tag{9}$$

This article has been accepted for publication in a future issue of this journal, but has not been fully edited. Content may change prior to final publication. Citation information: DOI 10.1109/TMI.2016.2536779, IEEE Transactions on Medical Imaging

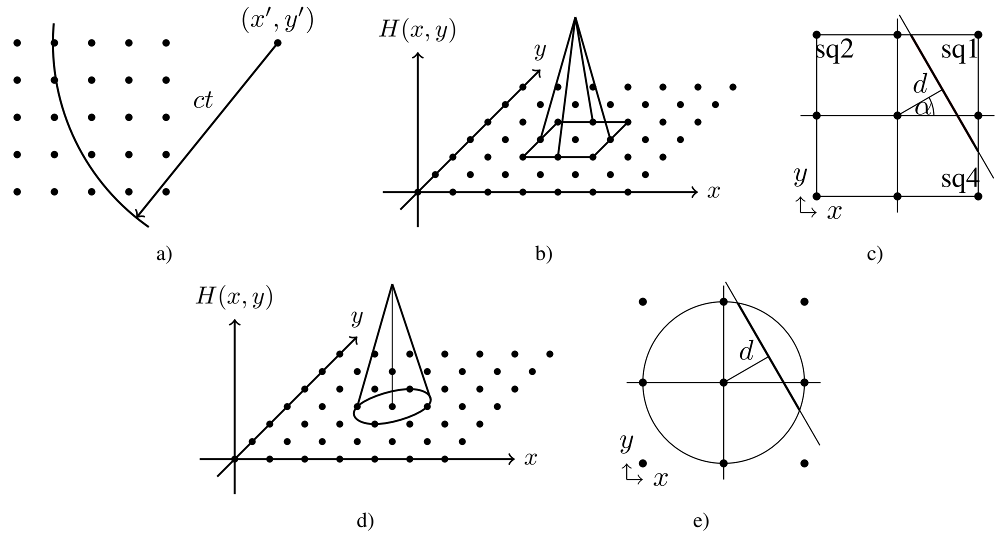

Fig. 1: Illustration of the discretization procedure for the cross-sectional (two-dimensional) optoacoustic imaging problem. a) Discretization of the forward model on a Cartesian grid using b) c) bilinear interpolation and d) e) circular interpolation.

or, equivalently

$$p_i(\boldsymbol{r}', t) = -\frac{c}{(s-d)^2} I(d,\alpha) - \frac{c}{s-d} dI(d,\alpha), \tag{10}$$

where

$$I(d,\alpha) = \int_{L(t)} K(\boldsymbol{r} - \boldsymbol{r}_i) dL(t), \tag{11}$$

$$dI(d,\alpha) = \frac{\partial}{\partial d} \int_{L(t)} K(\boldsymbol{r} - \boldsymbol{r}_i) dL(t). \tag{12}$$

Taking into account that $dI(d,\alpha)$ is in the order of $\frac{max[I(d,\alpha)]}{\Delta xy}$, the first term in (10) can be neglected, leading to

$$p_i(\boldsymbol{r}', t) = -\frac{c}{s-d} dI(d,\alpha), \tag{13}$$

where $dI(d,\alpha)$ does not depend on the pixel position $\boldsymbol{r}_i$ and can be thus expressed analytically (see Appendix A for a detailed derivation).

2) Circular interpolation: The calculation of the optical absorption distribution at any point can be further simplified by interpolating in a circular neighborhood of each pixel. In this case, the interpolation function is represented instead by the cone shown in Fig. 1 d). The circular interpolation function is then given by

$$K(\boldsymbol{r} - \boldsymbol{r}_i) = \begin{cases} 0 & |\boldsymbol{r} - \boldsymbol{r}_i| \geqslant \Delta xy \\ 1 - \frac{|\boldsymbol{r} - \boldsymbol{r}_i|}{\Delta xy} & |\boldsymbol{r} - \boldsymbol{r}_i| < \Delta xy \end{cases}. \tag{14}$$

As a result, the derivative $dI(d,\alpha)$ in (9) for the circular interpolation is independent of the angle α and only depends on the distance d (Fig. 1 e). Therefore, $p_i(\boldsymbol{r}', t)$ can be expressed as

$$p_i(\boldsymbol{r}', t) = -\frac{c}{s-d} dI(d). \tag{15}$$

See Appendix B for more details on the calculation of $dI(d)$ in (15).

C. Image reconstruction

Optoacoustic tomographic reconstruction implies processing the pressure signals collected at a set of transducer locations $\boldsymbol{r}'_1, \cdots, \boldsymbol{r}'_L$ and time instants $t_1, \cdots, t_K$.Let

$$\boldsymbol{p}_{ij} = \begin{pmatrix} p_i(\boldsymbol{r}'_j, t_1) \\ \vdots \\ p_i(\boldsymbol{r}'_j, t_K) \end{pmatrix} \tag{16}$$

represent the theoretical pressure signal for the considered instants at position $\boldsymbol{r}'_j$ generated by a unit absorber at pixel i and

$$\boldsymbol{h} = \begin{pmatrix} H(\boldsymbol{r}_1) \\ \vdots \\ H(\boldsymbol{r}_N) \end{pmatrix} \tag{17}$$

denote a vector representing optical absorption at the pixels $1, \cdots, N$ of the reconstruction grid. By considering (6), a linear model

$$\boldsymbol{p} = \boldsymbol{A}\boldsymbol{h} \tag{18}$$

can be defined with the model matrix expressed as

$$\boldsymbol{A} = [\boldsymbol{a}_1, \cdots, \boldsymbol{a}_N], \tag{19}$$

where

$$\boldsymbol{a}_i = \begin{pmatrix} \boldsymbol{p}_{i1} \\ \vdots \\ \boldsymbol{p}_{iL} \end{pmatrix}. \tag{20}$$

Image reconstruction is then done by minimizing the least squared error between the measured signals in a vector form $\boldsymbol{p}_m$ and the corresponding signals predicted by the forward model, i.e.,

$$\hat{\boldsymbol{h}} = \arg\min_{\boldsymbol{h}} \|\boldsymbol{p}_m - \boldsymbol{A}\boldsymbol{h}\|_2. \tag{21}$$

The least squared inversion problem in (21) can be solved with iterative methods such as LSQR [38], which requires one calculation of a matrix-vector multiplication with the model

This article has been accepted for publication in a future issue of this journal, but has not been fully edited. Content may change prior to final publication. Citation information: DOI 10.1109/TMI.2016.2536779, IEEE Transactions on Medical Imaging

matrix, $\boldsymbol{Av}$, and one multiplication with its transpose, $\boldsymbol{A}^\top\boldsymbol{u}$, in each iteration. The vectors $\boldsymbol{v}$ and $\boldsymbol{u}$ are updated in each iteration of the LSQR algorithm using the results of the matrix-vector products.

An additional regularization term may be included in (21). However, no regularization is required in the LSQR inversion of the two dimensional model provided sufficient angular coverage is available in the cross-sectional optoacoustic tomographic imaging system [21].

D. GPU implementation

The most computationally demanding operations in the above mentioned iterative inversion procedure are associated with the matrix-vector multiplications $\boldsymbol{Av}$ and $\boldsymbol{A}^\top\boldsymbol{u}$. Those operations can be significantly accelerated by a GPU-based implementation, which can generally be done in various ways. The most straightforward approach consists in the precalculation of the model matrix $\boldsymbol{A}$ and its subsequent storage on the GPU memory. Despite the sparsity of $\boldsymbol{A}$, this approach is hindered by the relatively small internal memory resources available on the GPUs, which may turn insufficient for storing model matrices corresponding to the required number of image pixels, simultaneously detected signals and their temporal sampling resolution. This limitation is particularly relevant for high-resolution reconstructions or three-dimensional inversions [37], [39] employing very large model matrices. For instance, the model matrix in the examples shown later in this work (i.e., with 256 channels, 732 sampling instants and 200x200 pixels) occupies around 300 MB of memory in a sparse representation. The memory needed is increased several orders of magnitude for a non-sparse representation. Standard GPUs have an internal memory of around 1-4 GB, which is enough to store the entire model-matrix for the reconstruction examples shown in this paper. However, it can be insufficient for reconstructions with a higher resolution, number of channels or sampling instants. On the other hand, the memory requirements exponentially increase for three-dimensional reconstructions, where the model matrix generally occupies many tens of GBs of memory. Another approach consists in on-the-fly calculation of the elements of the model matrix in each iteration of the inversion procedure [27]. This approach is widely applicable as no storage is required, but the required computational time is generally longer due to the need to repeat the same operations multiple times.

We propose an alternative approach based on the precalculation and storage of a small look-up table containing the derivatives $dI(d,\alpha)$ and $dI(d)$ in (13) and (15) corresponding to the different values of d and α. Such table can readily be stored in the GPU memory, and the calculation of the elements of the model matrix simply involves divisions and multiplications. As opposed to the large amount of memory that may be required for storing the entire model matrix on a GPU, the precalculated look-up tables for dI only occupy 800 Byte and 156 KB of memory for the bilinear and circular interpolation methods, respectively (for 200 different values of d and 200 different values of α). Since $\boldsymbol{A}$ is highly sparse, $\boldsymbol{Av}$ and $\boldsymbol{A}^\top\boldsymbol{u}$ can be subsequently obtained by calculating only the non-zero elements and multiplying them with the corresponding elements of the vectors $\boldsymbol{v}$ and $\boldsymbol{u}$. The matrix vector multiplications $\boldsymbol{Av}$ and $\boldsymbol{A}^\top\boldsymbol{u}$ are calculated row-wise and in parallel. In the calculation of $\boldsymbol{A}^\top\boldsymbol{u}$, each computing unit (kernel) calculates a value for each of the N pixels, namely the multiplication of non-zero elements of $\boldsymbol{a}_i$ [cf. (19)] with the corresponding elements in vector $\boldsymbol{u}$. In calculating $\boldsymbol{Av}$, each computing unit performs the operations corresponding to one transducer position and one sampling instant, i.e. the multiplication of non-zero elements of $\left[p_1(\boldsymbol{r}'_j,t_k),\cdots,p_N(\boldsymbol{r}'_j,t_k)\right]$ [cf. (13) (15)] with their corresponding elements in vector $\boldsymbol{v}$. The specific steps for the parallel implementation of these operations are illustrated in Appendix C. In a practical implementation, the symmetry of the bilinear interpolation function can be exploited to reduce the storage requirement for the lookup table (see Appendix A).

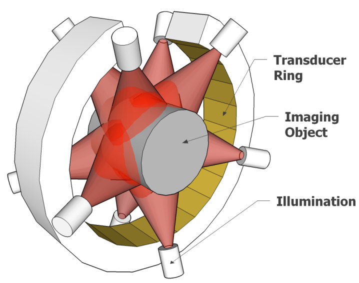

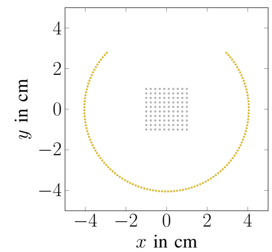

Fig. 2: Illustration of the experimental cross-sectional optoacoustic tomography system. a) Three-dimensional representation of the actual experimental system. b) Geometrical distribution of transducer locations (gold dots) and Cartesian grid (gray dots) considered for two dimensional reconstruction.

Further acceleration of the reconstruction process is possible if multiple images are simultaneously reconstructed since the matrix elements are only calculated once for all the reconstructed images. This approach is convenient for off-line reconstructions but not appropriate for real-time imaging since, in the latter case, the reconstruction must be accomplished in between the consecutive signal acquisitions.

E. Experimental measurements

The performance of the proposed model-based reconstruction approach was examined with experimental data acquired from mice. For this, a small animal optoacoustic tomography system (MSOT256-TF, iThera Medical GmbH, Munich, Germany) was used, which is based on signal acquisition with 256-element arc-shaped array of cylindrically-focused transducers covering 270° around the imaged object [40]. The system attains ring-type illumination on the surface of the imaged object by means of a fiber bundle. An illustration of the system is shown in Fig. 2. The acquired signals were digitized at 40 megasamples per second and band-pass filtered with cut-off frequencies 0.1 and 7 MHz.

The proposed algorithm using both interpolation methods was first compared to a reference model-based reconstruction algorithm [20]. Then, the inversion performance was evaluated as a function of various parameters, such as number of LSQR iterations, number of projections and number of sampling time instants in the acquired signal (time resolution). As a reference, we considered the image reconstructed with bilinear interpolation, 20 LSQR iterations, 256 projections and 1098 time instants. Finally, the reconstruction times of bilinear interpolation and circular interpolation were compared both for single frame and multiple frame reconstructions using the optimum parameters. All images were reconstructed with 200x200 pixels.

The reconstruction was done on a AMD Radeon HD 7900 series GPU with 3GB on-board memory and 32 computing units (2048 stream processors). The reconstruction was implemented using the OpenCL framework and executed in Matlab (MathWorks, Natick, MA) as a mex function.

III. Results

The cross-sectional images of the mice in the kidney/spleen and liver regions are shown in Fig. 3. The images in Fig. 3 a) and g) were reconstructed with a previously introduced model-based algorithm [20]. The reconstructed images obtained by using the proposed algorithm with bilinear interpolation and circular interpolation are plotted in Fig. 3 b) h) and Fig. 3 c) i) respectively. Fig. 3 d)-f) show close-up images of the blue rectangular regions in a)-c). No significant difference in the imaged small structures in the kidney regions can be observed in the three images. For all three approaches, the accquired pressure signals were cut and downsampled to 1098 time instants prior to reconstruction. All 256 projections were considered and the number of LSQR iterations were set to 10. Fig. 3 j) shows the signal to noise ratios (SNR) of Fig. 3 a)-c) and g)-i) calculated with the absorption values in the squared regions marked in Fig. 3 a) and g). Specifically, the SNR was calculated as the maximum reconstructed absorption in a region inside the mouse normalized to the standard deviation of the reconstructed absorption in a region outside the mouse. The obtained SNR of the kidney images a) to c) were 18.7744, 18.8475 and 18.7727 and the calculated SNR of the liver images g) to i) were 21.7461, 21.9314 and 20.6545. No essential differences between the reconstructed images using the three approaches can be observed.

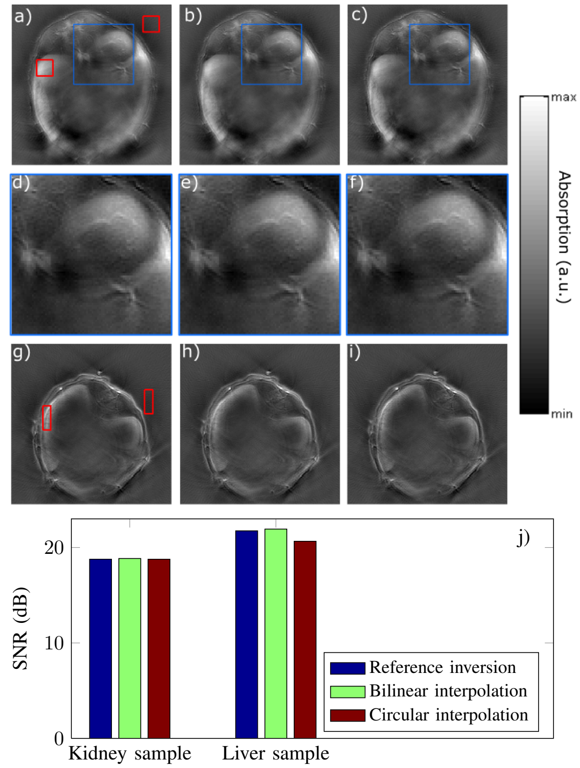

Fig. 3: Cross-sectional images acquired from a mouse in the kidney and liver regions. a) and g) are reconstructed using the standard iterative model-based inversion. Reconstructions using the proposed algorithm are shown in b) and h) for the bilinear interpolation and c) and i) for the circular interpolation respectively. d)-f) close-up images of the corresponding blue regions in a)-c). j) SNR performance of the different reconstruction schemes.

For the purpose of evaluting the image quality of reconstructed images using different parameters, we used the reference image shown in Fig. 4 e), which is obtained as described in Section 2.5. The relative error is calculated as the norm of the difference with the reference image normalized with the norm of the reference image. Fig. 4 a)-d) show examples of images with increasing numbers of iterations, yielding resulting relative errors of 58.5%, 37.5%, 17.8% and 13% respectively. The differences of Fig. 4 a) d) with respect to the reference image are displayed in Fig. 4 f)-i). Minor differences can be seen in h) and i), which indicates acceptable image quality is achieved for a relative error below 20%.

The relative error and the reconstruction time are shown as a function of the number of LSQR iterations in Fig. 5 a) and Fig. 5 b) for the bilinear interpolation and the circular interpolation approaches respectively. The corresponding normalized errors with both methods are reduced to approximately 13% and 15% after 5 LSQR iterations respectively, which was considered an acceptable performance. On the other hand, a two-fold reduction in the reconstruction time is achieved with circular interpolation as compared with the bilinear interpolation approach for the same number of iterations. The relative error and reconstruction time with respect to the number of projections (detector positions) are further presented in Fig. 5 c) and d) for the two interpolation methods. For a given number of projections, virtual signals were obtained by interpolating between the original 256 detection channels, while the angular coverage was maintained in all cases. 5 LSQR iterations were performed in the reconstruction. Note that a decrease in the number of projection leads to a significant increase in the error. Therefore, all 256 channels should be used to optimize the image quality for the number of pixels considered [41]. The performance results for different number of time instants are shown in Fig. 5 e) and f) for the two interpolation approaches. The reconstruction was done with 5 LSQR iterations and 256 projections. The length of the signals was fixed to 30 μs in all cases. For both interpolation approaches, no significant further improvement was achieved when increasing the number of time samples beyond 700.

This article has been accepted for publication in a future issue of this journal, but has not been fully edited. Content may change prior to final publication. Citation information: DOI 10.1109/TMI.2016.2536779, IEEE Transactions on Medical Imaging

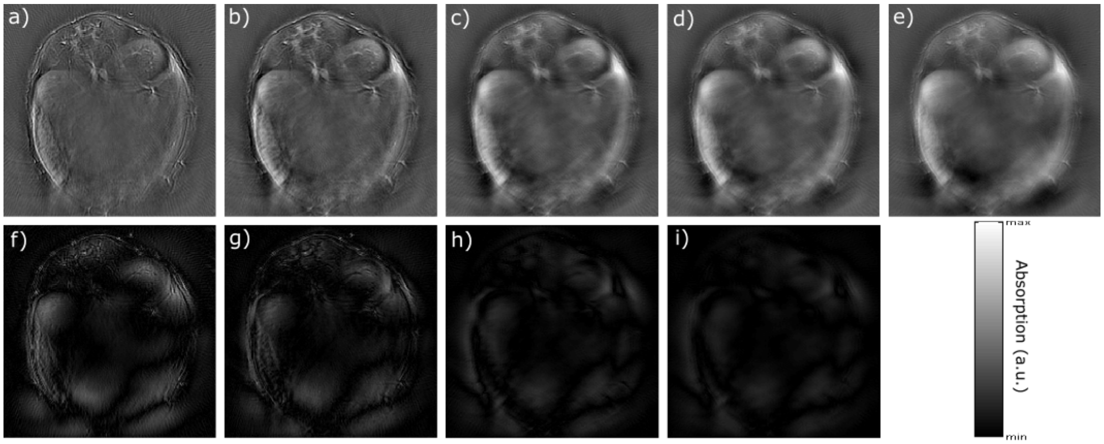

Fig. 4: Estimated relative errors. a) - d) are images reconstructed with 1, 2, 4, and 5 iterations, respectively, using the on-the-fly matrix calculation algorithm. Comparison to the reference image in e), reconstructed with the standard model-based algorithm with 20 iterations, results in estimated relative errors of 58.5%, 37.5%, 17.8%, and 13%, respectively. f) - i) Differences between the reference image and the images in a) - d).

	Bilinear intropolation	Circular interpolation
Single frame recon.	6 frames/s	13 frames/s
Multiple frame recon.	21 frames/s	27 frames/s

TABLE I: Performance of the single- and multiple-frame reconstructions using bilinear and circular interpolation approaches.

The performance of the proposed algorithm is summarized in TABLE I. The reconstruction parameters were selected according to the results presented in Fig. 5 so that the reconstruction time is optimized without compromising image quality. Specifically, the number of LSQR iterations was set to 5, all 256 projections were taken and the signals were downsampled to 732 time instants. As shown in the table, it was possible to achieve 6 and 13 frames per second for single frame reconstruction by employing the bilinear and circular interpolation models respectively. When applying the multiple frame reconstruction approach 21 and 27 frames could be reconstructed simultaneously within one second with the two interpolation approaches. As a reference, standard model-based reconstruction on the CPU using the same parameters needs around 94s to build the model-matrix and 0.9s to reconstruct one frame on an Intel Core i7-4820K CPU @ 3.7GHz.

IV. Discussion and Conclusions

Model-based reconstruction approaches are generally known to render better image quality and accuracy as compared to the approximate analytical inversion schemes [37], [39]. Yet, the analytical (closed-form) inversion schemes have been so far the dominant approach for image reconstruction in optoacoustic tomography due to their fast reconstruction abilities and low memory requirements [28]. In this work, a novel discretization procedure for model-based reconstruction in two-dimensional (cross-sectional) optoacoustic tomography has been introduced. The suggested method allows for parallel implementation on a GPU with relatively low complexity, which is achieved by on-the-fly calculation of the model matrix in each iteration of the inversion procedure. Parallelization and acceleration of the reconstruction on a GPU are equally possible with the other model-based approaches, such as those using pre-calculation of the model matrix. However, memory limitations may restrict applicability of the latter approaches, especially when handling dense image grids or large number of voxels in three-dimensional reconstructions. In contrast, applicability of our methodology does not depend on the size of the model matrix as it only requires the storage of a small look-up table on the GPU memory. Moreover, the look-up table approach signicantly accelerates the on-the-fly computation of the matrix elements as only one additional multiplication and division are needed. Here two interpolation approaches were proposed and analyzed. It was demonstrated that reconstructions based on circular interpolation yield slightly reduced image quality as compared to the bilinear interpolation method, yet attain twice the reconstructed frame rates exceeding 10 frames per second for a two-dimensional grid of 200x200 pixels. The suggested reconstruction method was additionally demonstrated to reconstruct multiple frames simultanouly, in which case imaging rate exceeding 20 frames per second were achieved. This performance matches well the pulse repetition and spatial resolution parameters of some common real-time optoacoustic tomography systems for small animal imaging [33], [42]. Yet, the plea for real-time performance is of particular importance when considering clinical translation of the optoacoustic technology using hand-held probes [43], [44]. The proposed framework can further be extended to three-dimensional model-based reconstructions. In this case, the integral in the forward model is performed along a spherical surface instead of a circumference, thus the integration path in the neighborhood of each pixel can be approximated as a plane instead of a straight line. Our future work will address the three-dimensional problem with the suggested methodology in order to further demonstrate the benefits of this approach.

This article has been accepted for publication in a future issue of this journal, but has not been fully edited. Content may change prior to final publication. Citation information: DOI 10.1109/TMI.2016.2536779, IEEE Transactions on Medical Imaging

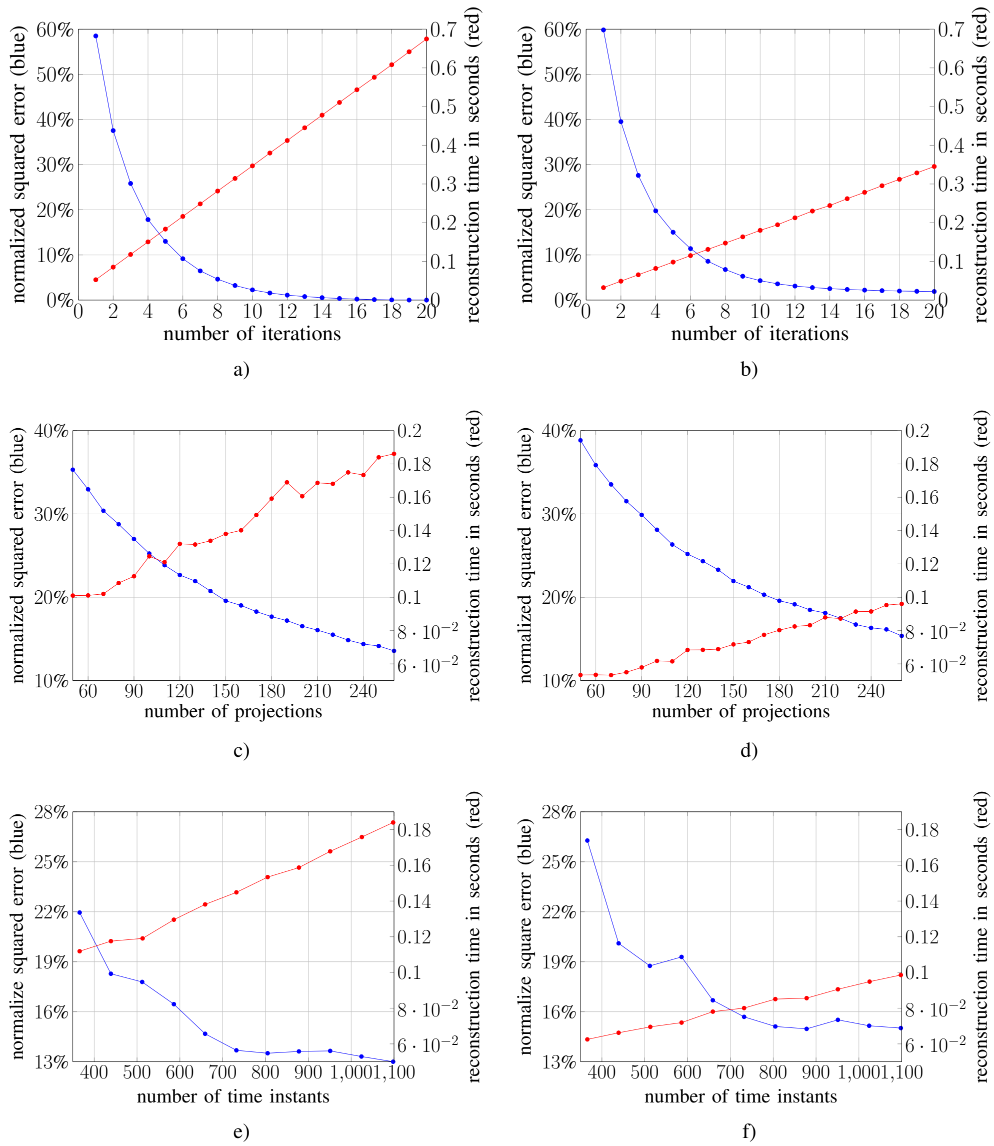

Fig. 5: Influence of different parameters on the image quality and reconstruction speed. Left and right columns show results for the bilinear and circular interpolations, respectively. We vary a)-b) the number of iterations, c)-d) the number of projections and e)-f) the number of time instants.

Acknowledgment

D. R. acknowledges support from the European Research Council under grant agreement ERC-2010-StG-260991.

Appendix

A. Bilinear interpolation

We derive in this section the analytical expression for $dI(d, \alpha)$ for the bilinear interpolation approach. Due to the symmetry of bilinear interpolation in a square grid it is verified that

$$dI(d, \alpha) = -dI(-d, \alpha), \tag{22}$$

and

$$dI(d, \alpha) = dI(d, \alpha'), \tag{23}$$

being

$$\alpha' = \min\left(|\alpha|, |\alpha - \frac{\pi}{2}|, |\alpha - \pi|, |\alpha - \frac{3\pi}{2}|\right). \tag{24}$$

Then, we only need to derive the analytical expression for $d \geqslant 0$ and for $0 \leqslant \alpha \leqslant \frac{\pi}{4}$. In that case, it can be expressed as a linear combination of the derivative of the integral in the squares indicated in Fig. 1 c).

$$dI(d, \alpha) = dI_{\text{sq1}}(d, \alpha) + dI_{\text{sq2}}(d, \alpha) + dI_{\text{sq4}}(d, \alpha). \tag{25}$$

The straight line along which the integral is calculated can be expressed as

$$x(y) = \frac{d}{\cos\alpha} - y \tan\alpha, \tag{26}$$

This article has been accepted for publication in a future issue of this journal, but has not been fully edited. Content may change prior to final publication. Citation information: DOI 10.1109/TMI.2016.2536779, IEEE Transactions on Medical Imaging

where $(x,y)=(0,0)$ represents the position of the pixel. With

$$\widetilde{dI}_{\text{sq1}} = \frac{\partial}{\partial d}\int\limits_{y_a}^{y_b} \frac{(\Delta xy - x(y))(\Delta xy - y)}{\Delta xy^2}\frac{dy}{\cos\alpha}, \tag{27}$$

we have

$$dI_{\text{sq1}}(d,\alpha) = \begin{cases}\widetilde{dI}_{\text{sq1}} & \text{for } 0 \leqslant d < \sqrt{2}\Delta xy\cos\left(\frac{\pi}{4}-\alpha\right) \\ 0 & \text{for } d \geqslant \sqrt{2}\Delta xy\cos\left(\frac{\pi}{4}-\alpha\right)\end{cases}. \tag{28}$$

The integration limits y_a and y_b correspond to

$$y_a = \begin{cases}\widetilde{y}_{a,\text{sq1}} & \text{for } \Delta xy\cos\alpha \leqslant d < \sqrt{2}\Delta xy\cos\left(\frac{\pi}{4}-\alpha\right) \\ 0 & \text{for } \Delta xy\sin\alpha \leqslant d < \Delta xy\cos\alpha \\ 0 & \text{for } 0 \leqslant d < \Delta xy\sin\alpha\end{cases}, \tag{29}$$

with

$$\widetilde{y}_{a,\text{sq1}} = \frac{d}{\sin\alpha} - \tan\left(\frac{\pi}{2}-\alpha\right)\Delta xy, \tag{30}$$

and

$$y_b = \begin{cases}\Delta xy & \text{for } \Delta xy\cos\alpha \leqslant d < \sqrt{2}\Delta xy\cos\left(\frac{\pi}{4}-\alpha\right) \\ \Delta xy & \text{for } \Delta xy\sin\alpha \leqslant d < \Delta xy\cos\alpha \\ \frac{d}{\sin\alpha} & \text{for } 0 \leqslant d < \Delta xy\sin\alpha\end{cases}. \tag{31}$$

With

$$\widetilde{dI}_{\text{sq2}} = \frac{\partial}{\partial d}\int\limits_{y_a}^{y_b} \frac{(\Delta xy + x(y))(\Delta xy - y)}{\Delta xy^2}\frac{dy}{\cos\alpha}, \tag{32}$$

we have

$$dI_{\text{sq2}}(d,\alpha) = \begin{cases}\widetilde{dI}_{\text{sq2}} & \text{for } 0 \leqslant d < \Delta xy\sin\alpha \\ 0 & \text{for } d \geqslant \Delta xy\sin\alpha\end{cases}. \tag{33}$$

In this case, the integration limits y_a and y_b are given by

$$y_a = \frac{d}{\sin\alpha} \quad \text{for } 0 \leqslant d < \Delta xy\sin\alpha \tag{34}$$

and

$$y_b = \Delta xy \quad \text{for } 0 \leqslant d < \Delta xy\sin\alpha. \tag{35}$$

Finally, with

$$\widetilde{dI}_{\text{sq4}} = \frac{\partial}{\partial d}\int\limits_{y_a}^{y_b} \frac{(\Delta xy - x(y))(\Delta xy + y)}{\Delta xy^2}\frac{dy}{\cos\alpha}, \tag{36}$$

we have

$$dI_{\text{sq4}}(d,\alpha) = \begin{cases}\widetilde{dI}_{\text{sq4}} & \text{for } 0 \leqslant d < \Delta xy\cos\alpha \\ 0 & \text{for } d \geqslant \Delta xy\cos\alpha\end{cases}. \tag{37}$$

The integration limits y_a and y_b can be expressed as

$$y_a = \begin{cases}\widetilde{y}_{a,\text{sq4}} & \text{for } \sqrt{2}\Delta xy\sin\left(\frac{\pi}{4}-\alpha\right) \leqslant d < \Delta xy\cos\alpha \\ -\Delta xy & \text{for } 0 \leqslant d < \sqrt{2}\Delta xy\sin\left(\frac{\pi}{4}-\alpha\right)\end{cases}, \tag{38}$$

with

$$\widetilde{y}_{a,\text{sq4}} = \frac{d}{\sin\alpha} - \tan\left(\frac{\pi}{2}-\alpha\right)\Delta xy, \tag{39}$$

and

$$y_b = \begin{cases}0 & \text{for } \sqrt{2}\Delta xy\sin\left(\frac{\pi}{4}-\alpha\right) \leqslant d < \Delta xy\cos\alpha \\ 0 & \text{for } 0 \leqslant d < \sqrt{2}\Delta xy\sin\left(\frac{\pi}{4}-\alpha\right)\end{cases}. \tag{40}$$

The exact analytical expressions for $dI(d,\alpha)$ are then calculated with the symbolic toolbox of Matlab and are not displayed here due to its complexity.

B. Circular interpolation

We derive in this section the analytical expression for $dI(d)$ for the circular interpolation approach. The integral along the straight line within the round neighborhood of a pixel equals the area of intersection of a vertical plane cutting the cone illustrated in Fig. 1 d). Since the cone is circularly symmetric, we consider the integral along the straight line $x=d$ without loss of generality. We assume that the distance d is normalized by the pixel size Δxy. The function value of the cone with diameter one along $x=d$ is given by

$$f(y) = \begin{cases}1-\sqrt{y^2+d^2} & \text{for } |y| < \sqrt{1-d^2} \\ 0 & \text{otherwise}\end{cases}. \tag{41}$$

The area integral is thus given by

$$2\sqrt{1-d^2} - \int\limits_{-\sqrt{1-d^2}}^{\sqrt{1-d^2}} \sqrt{y^2+d^2}dy = \sqrt{1-d^2} + \frac{1}{2}d^2\left(\log\left(1-\sqrt{1-d^2}\right) - \log\left(1+\sqrt{1-d^2}\right)\right). \tag{42}$$

Consequently, the derivative of integral dI can be obtained by differentiating (42) with respect to d

$$dI(d) = d\left(\log\left(1-\sqrt{1-d^2}\right) - \log\left(1+\sqrt{1-d^2}\right)\right). \tag{43}$$

C. GPU implementation

The detailed implementations of $\boldsymbol{A}^\mathsf{T}\boldsymbol{u}$ and $\boldsymbol{A}\boldsymbol{v}$ on the GPU kernel are described in Alg. 1 and Alg. 2. Note that we only demonstrate the implementation of the bilinear interpolation since the implementation of the circular interpolation is almost identical.

REFERENCES

[1] G Paltauf, JA Viator, SA Prahl, and SL Jacques. Iterative reconstruction algorithm for optoacoustic imaging. *The Journal of the Acoustical Society of America*, 112(4):1536–1544, 2002.

[2] Minghua Xu and Lihong V. Wang. Universal back-projection algorithm for photoacoustic computed tomography. *Phys. Rev. E*, 71:016706, Jan 2005.

[3] Bradley E Treeby and Benjamin T Cox. k-wave: Matlab toolbox for the simulation and reconstruction of photoacoustic wave fields. *Journal of biomedical optics*, 15(2):021314–021314, 2010.

[4] Yulia Hristova, Peter Kuchment, and Linh Nguyen. Reconstruction and time reversal in thermoacoustic tomography in acoustically homogeneous and inhomogeneous media. *Inverse Problems*, 24(5):055006, 2008.

[5] Rainer Schulze, Gerhard Zangerl, Markus Holotta, Dirk Meyer, Florian Handle, Robert Nuster, GÃžnther Paltauf, and Otmar Scherzer. On the use of frequency-domain reconstruction algorithms for photoacoustic imaging. *Journal of biomedical optics*, 16(8):086002–086002, 2011.

This article has been accepted for publication in a future issue of this journal, but has not been fully edited. Content may change prior to final publication. Citation information: DOI 10.1109/TMI.2016.2536779, IEEE Transactions on Medical Imaging

Algorithm 1: Implementation of kernel $\boldsymbol{A}^\mathsf{T}\boldsymbol{u}$

Input : $\boldsymbol{u}$: input vector
c: speed of sound
Δxy: pixel width
L: number of transducers
$\boldsymbol{r}'_1, \cdots, \boldsymbol{r}'_L$: transducer locations
$\boldsymbol{r}_i$: location of pixel i
$\boldsymbol{t}$: time instant vector
dI_{Table}: lookup table for dI values
Output: $(\boldsymbol{A}^\mathsf{T}\boldsymbol{u})_i$
$(\boldsymbol{A}^\mathsf{T}\boldsymbol{u})_i \leftarrow 0$
for $\ell = 1$ **to** L **do**
  $\boldsymbol{w} \leftarrow \boldsymbol{r}'_\ell - \boldsymbol{r}_i$
  $s \leftarrow |\boldsymbol{w}|$
  $n_1 \leftarrow \left\lfloor \frac{-t_0 + \frac{s-\sqrt{2}\Delta xy}{c}}{t_1 - t_0} \right\rfloor$
  $n_2 \leftarrow \left\lceil \frac{-t_0 + \frac{s+\sqrt{2}\Delta xy}{c}}{t_1 - t_0} \right\rceil$
  for $k = n_1$ **to** n_2 **do**
    $\alpha \leftarrow \arctan(\frac{\boldsymbol{w}_y}{\boldsymbol{w}_x})$
    $d \leftarrow s - ct_k$
    $dI \leftarrow dI_{Table}(d, \alpha)$
    $(\boldsymbol{A}^\mathsf{T}\boldsymbol{u})_i \leftarrow (\boldsymbol{A}^\mathsf{T}\boldsymbol{u})_i - [\boldsymbol{u}]_k \frac{c}{s-d} dI$

Algorithm 2: Implementation of kernel $\boldsymbol{A}\boldsymbol{v}$. Note that all coordinates are with respect to the lower left corner of the reconstructed image such that the pixel in row m and column j is at position $r_x = m\Delta xy$ and $r_y = j\Delta xy$

Input : $\boldsymbol{v}$: input vector
c: speed of sound
n: width of the picture in pixels
Δxy: pixel width
$\boldsymbol{r}'_\ell$: transducer location
t: time instant
dI_{Table}: lookup table for dI values
Output: $(\boldsymbol{A}\boldsymbol{v})_\ell$
$(\boldsymbol{A}\boldsymbol{v})_\ell \leftarrow 0$
for $m = 0$ **to** $n - 1$ **do**
  For each row m calculate the intersections of the line $x = m\Delta xy$ with the rings around $\boldsymbol{r}'_\ell$ with radiuses $ct + \sqrt{2}\Delta xy$ and $ct - \sqrt{2}\Delta xy$.
  if *No intersection* **then**
    continue
  if *only the outer ring intersects at* y_1 *and* y_2 *with* $y_1 < y_2$ **then**
    $j_1 \leftarrow \lfloor y_1/\Delta xy \rfloor$
    $j_2 \leftarrow \lceil y_2/\Delta xy \rceil$
  else if *Four intersection points* $y_1 < y_2 < y_3 < y4$ **then**
    $j_1 \leftarrow \lfloor y_1/\Delta xy \rfloor$
    $j_2 \leftarrow \lceil y_2/\Delta xy \rceil$
    $j_3 \leftarrow \lfloor y_3/\Delta xy \rfloor$
    $j_4 \leftarrow \lceil y_4/\Delta xy \rceil$
  for $j = j_1, \ldots, j_2, j_3, \ldots, j_4$ *and* $0 \leq j \leq n-1$ **do**
    $i \leftarrow$ linear index of the pixel in row m and column j
    $\boldsymbol{w} \leftarrow \boldsymbol{r}'_\ell - \boldsymbol{r}_i$
    $s \leftarrow |\boldsymbol{w}|$
    $\alpha \leftarrow \arctan(\frac{\boldsymbol{w}_y}{\boldsymbol{w}_x})$
    $d \leftarrow s - ct$
    $dI \leftarrow dI_{Table}(d, \alpha)$
    $(\boldsymbol{A}\boldsymbol{v})_\ell \leftarrow (\boldsymbol{A}\boldsymbol{v})_\ell - [\boldsymbol{v}]_i \frac{c}{s-d} dI$

[6] Pouyan Mohajerani, Stephan Kellnberger, and Vasilis Ntziachristos. Frequency domain optoacoustic tomography using amplitude and phase. *Photoacoustics*, 2(3):111–118, 2014.

[7] Kornel P Köstli, Daniel Frauchiger, Joël J Niederhauser, Günther Paltauf, Heinz P Weber, and Martin Frenz. Optoacoustic imaging using a three-dimensional reconstruction algorithm. *Selected Topics in Quantum Electronics, IEEE Journal of*, 7(6):918–923, 2001.

[8] Kun Wang, Sergey Ermilov, Richard Su, Hans-Peter Brecht, Alexander Oraevsky, Mark Anastasio, et al. An imaging model incorporating ultrasonic transducer properties for three-dimensional optoacoustic tomography. *Medical Imaging, IEEE Transactions on*, 30(2):203–214, 2011.

[9] Kenji Mitsuhashi, Kun Wang, and Mark A Anastasio. Investigation of the far-field approximation for modeling a transducer's spatial impulse response in photoacoustic computed tomography. *Photoacoustics*, 2(1):21–32, 2014.

[10] Christian Lutzweiler and Daniel Razansky. Optoacoustic imaging and tomography: reconstruction approaches and outstanding challenges in image performance and quantification. *Sensors*, 13(6):7345–7384, 2013.

[11] Amir Rosenthal, Vasilis Ntziachristos, and Daniel Razansky. Acoustic inversion in optoacoustic tomography: A review. *Current medical imaging reviews*, 9(4):318, 2013.

[12] Lu Ding, X Luís Deán-Ben, Christian Lutzweiler, Daniel Razansky, and Vasilis Ntziachristos. Efficient non-negative constrained model-based inversion in optoacoustic tomography. *Physics in medicine and biology*, 60(17):6733, 2015.

[13] X Luís Deán-Ben, Daniel Razansky, and Vasilis Ntziachristos. The effects of acoustic attenuation in optoacoustic signals. *Physics in medicine and biology*, 56(18):6129, 2011.

[14] X Luís Deán-Ben, Vasilis Ntziachristos, and Daniel Razansky. Effects of small variations of speed of sound in optoacoustic tomographic imaging. *Medical physics*, 41(7):073301, 2014.

[15] Moritz Kneipp, Jake Turner, Héctor Estrada, Johannes Rebling, Shy Shoham, and Daniel Razansky. Effects of the murine skull in optoacoustic brain microscopy. *Journal of biophotonics*, 9999, 2015.

[16] Amir Rosenthal, Vasilis Ntziachristos, and Daniel Razansky. Model-based optoacoustic inversion with arbitrary-shape detectors. *Medical physics*, 38(7):4285–4295, 2011.

[17] Daniel Queirós, Xosé Luís Déan-Ben, Andreas Buehler, Daniel Razansky, Amir Rosenthal, and Vasilis Ntziachristos. Modeling the shape of cylindrically focused transducers in three-dimensional optoacoustic tomography. *Journal of biomedical optics*, 18(7):076014–076014, 2013.

[18] X Luís Deán-Ben, Rui Ma, Amir Rosenthal, Vasilis Ntziachristos, and Daniel Razansky. Weighted model-based optoacoustic reconstruction in acoustic scattering media. *Physics in medicine and biology*, 58(16):5555, 2013.

[19] Chao Huang, Liming Nie, Robert W Schoonover, Lihong V Wang, and Mark A Anastasio. Photoacoustic computed tomography correcting for heterogeneity and attenuation. *Journal of biomedical optics*, 17(6):0612111–0612115, 2012.

[20] X Luís Deán-Ben, Vasilis Ntziachristos, and Daniel Razansky. Acceleration of optoacoustic model-based reconstruction using angular image discretization. *Medical Imaging, IEEE Transactions on*, 31(5):1154–1162, 2012.

[21] Amir Rosenthal, Daniel Razansky, and Vasilis Ntziachristos. Fast semi-analytical model-based acoustic inversion for quantitative optoacoustic tomography. *Medical Imaging, IEEE Transactions on*, 29(6):1275–1285, 2010.

[22] Amir Rosenthal, Thomas Jetzfellner, Daniel Razansky, and Vasilis Ntziachristos. Efficient framework for model-based tomographic image reconstruction using wavelet packets. *Medical Imaging, IEEE Transactions on*, 31(7):1346–1357, 2012.

[23] Yiyong Han, Stratis Tzoumas, Antonio Nunes, Vasilis Ntziachristos, and Amir Rosenthal. Sparsity-based acoustic inversion in cross-sectional multiscale optoacoustic imaging. *Medical physics*, 42(9):5444–5452, 2015.

[24] Shuhui Bu, Zhenbao Liu, Tsuyoshi Shiina, Kengo Kondo, Makoto Yamakawa, Kazuhiko Fukutani, Yasuhiro Someda, and Yasufumi Asao. Model-based reconstruction integrated with fluence compensation for photoacoustic tomography. *Biomedical Engineering, IEEE Transactions on*, 59(5):1354–1363, 2012.

[25] Christian Lutzweiler, Xosé Luís Deán-Ben, and Daniel Razansky. Expediting model-based optoacoustic reconstructions with tomographic symmetries. *Medical physics*, 41(1):013302, 2014.

[26] Miguel Angel Araque Caballero, Jérôme Gateau, Xosé-Luis Déan-Ben, and Vasilis Ntziachristos. Model-based optoacoustic image reconstruction of large three-dimensional tomographic datasets acquired with an array of directional detectors. *Medical Imaging, IEEE Transactions on*, 33(2):433–443, 2014.

[27] Kun Wang, Chao Huang, Yu-Jiun Kao, Cheng-Ying Chou, Alexander A Oraevsky, and Mark A Anastasio. Accelerating image reconstruction in three-dimensional optoacoustic tomography on graphics processing units. *Medical physics*, 40(2):023301, 2013.

[28] X Luis Dean-Ben, Ali Ozbek, and Daniel Razansky. Volumetric real-time tracking of peripheral human vasculature with gpu-accelerated three-dimensional optoacoustic tomography. *Medical Imaging, IEEE Transactions on*, 32(11):2050–2055, 2013.

[29] Kun Wang, Jun Xia, Changhui Li, Lihong V Wang, and Mark A Anastasio. Fast spatiotemporal image reconstruction based on low-rank matrix estimation for dynamic photoacoustic computed tomography. *Journal of biomedical optics*, 19(5):056007–056007, 2014.

[30] Christian Lutzweiler, Stratis Tzoumas, Amir Rosenthal, Vasilis Ntziachristos, and Daniel Razansky. High-throughput sparsity-based inversion scheme for optoacoustic tomography. 2015.

[31] Jun Xia, Muhammad R Chatni, Konstantin Maslov, Zijian Guo, Kun Wang, Mark Anastasio, and Lihong V Wang. Whole-body ring-shaped confocal photoacoustic computed tomography of small animals in vivo. *Journal of biomedical optics*, 17(5):0505061–0505063, 2012.

[32] Liangzhong Xiang, Bo Wang, Lijun Ji, and Huabei Jiang. 4-d photoacoustic tomography. *Scientific reports*, 3, 2013.

[33] Xosé Luís Deán-Ben, Erwin Bay, and Daniel Razansky. Functional optoacoustic imaging of moving objects using microsecond-delay acquisition of multispectral three-dimensional tomographic data. *Scientific reports*, 4, 2014.

[34] Vitaliĭ Ėduardovich Gusev. *Laser optoacoustics*. Amer Inst of Physics, 1993.

[35] BT Cox, S Kara, SR Arridge, and PC Beard. k-space propagation models for acoustically heterogeneous media: Application to biomedical photoacoustics. *The Journal of the Acoustical Society of America*, 121(6):3453–3464, 2007.

[36] Lihong V Wang. *Photoacoustic imaging and spectroscopy*. CRC press, 2009.

[37] X Luís Dean-Ben, Andreas Buehler, Vasilis Ntziachristos, and Daniel Razansky. Accurate model-based reconstruction algorithm for three-dimensional optoacoustic tomography. *Medical Imaging, IEEE Transactions on*, 31(10):1922–1928, 2012.

[38] Christopher C Paige and Michael A Saunders. Lsqr: An algorithm for sparse linear equations and sparse least squares. *ACM Transactions on Mathematical Software (TOMS)*, 8(1):43–71, 1982.

[39] Kun Wang, Richard Su, Alexander A Oraevsky, and Mark A Anastasio. Investigation of iterative image reconstruction in three-dimensional optoacoustic tomography. *Physics in medicine and biology*, 57(17):5399, 2012.

[40] Daniel Razansky, Andreas Buehler, and Vasilis Ntziachristos. Volumetric real-time multispectral optoacoustic tomography of biomarkers. *Nature protocols*, 6(8):1121–1129, 2011.

[41] Alexander Dima, Neal C Burton, and Vasilis Ntziachristos. Multispectral optoacoustic tomography at 64, 128, and 256 channels. *Journal of biomedical optics*, 19(3):036021–036021, 2014.

[42] Lihong V Wang and Song Hu. Photoacoustic tomography: in vivo imaging from organelles to organs. *Science*, 335(6075):1458–1462, 2012.

[43] Alexander Dima and Vasilis Ntziachristos. Non-invasive carotid imaging using optoacoustic tomography. *Optics express*, 20(22):25044–25057, 2012.

[44] Andreas Buehler, Marcin Kacprowicz, Adrian Taruttis, and Vasilis Ntziachristos. Real-time handheld multispectral optoacoustic imaging. *Optics letters*, 38(9):1404–1406, 2013.